Furnace Operational Parameters and Reproducible Annealing of Thin Films

Victor Ovchinnikov
Department of Aalto Nanofab
School of Electrical Engineering, Aalto University
Espoo, Finland
e-mail: Victor.Ovchinnikov@aalto.fi

***Abstract*—Annealing of thin silver films on oxidized silicon substrates in different furnaces is studied. It is shown that identical temperatures and durations of thermal treatment do not guarantee reproducibility, i.e., the annealing provides different results, e.g., shape and size of nanostructures in different furnaces. To clarify the source of the variation, morphology and optical properties of the samples are analyzed. Spectroscopic ellipsometry is used to measure thickness and composition of the oxide layer before and after annealing. Reflectance spectra, obtained for different angles of incidence and polarizations, demonstrate the dependence of sample plasmonic properties on the furnace design. Additionally, a numerical simulation of the heating process in a diffusion furnace has been performed. It is concluded that uncontrollable overheating of silver film with regards to the substrate produced by thermal radiation of the environment leads to variation in annealing results.**

Keywords-silver thin film; diffusion furnace; annealing; nanostructures.

I. INTRODUCTION

Recently, the variation of annealing results for thin silver films heated at identical temperatures and during identical times has been demonstrated by using thermal processing tools of different designs [1].

Annealing is well known and broadly used in microfabrication for controlled heating of inorganic materials to alter their properties. In case of polymer, similar heat treatment is called baking, curing or drying. From the beginning of semiconductor technology, annealing has been used to modify properties of thin films, substrates and interfaces. Annealing is not a major microfabrication method like lithography or etching, however it is always included in fabrication of all micro- and nanodevices. The main application areas of annealing are doping of semiconductors, silicide formation, densification of deposited films, contact resistance decreasing, sample surface conditioning, etc. [2]. Annealing is done by heat treatment equipment, which can have completely different designs: convection and diffusion furnaces, hot plates and rapid thermal processing tools, infrared (IR) and curing ovens and so on. At the same time, annealing is usually characterized by only process temperature and time. Furthermore, temperature can be measured in different places: on a sample surface, in a fixed point of the heated volume, or on heating surfaces. Clearly, results of the annealing of the same samples, at the same time and temperature, but in various furnaces can be different. In this work, we anneal identical samples in identical conditions (time and temperature), but in different furnaces and study the effect of the furnace design on the obtained results.

The paper is organized as follows. In the subsequent Section II, the solved problem is formulated. In Section III, the details of sample preparation are given, the designs of three annealed furnaces are described and the measurement procedures are presented. In Section IV, the results of the work are demonstrated by scanning electron microscope (SEM) images, optical parameters of the layers obtained by spectroscopic ellipsometry, reflectance spectra of the samples for different angles of incidence and polarizations and also by a simulation of the heating process. The effect of furnace design on silver film annealing is discussed in Section V. In Section VI, the conclusions are drawn.

II. PROBLEM STATEMENT

The standard description of annealing in publications includes only temperature and duration of the process [3, 4]. Sometimes information about ambient or gas flow is added [5, 6]. The heat equipment and the sample position in the process chamber are rarely written about [7, 8]. However, different annealing tools deliver heat energy to a sample in different ways, which directly affects the obtained results.

During annealing heat exchange between the sample and a furnace is performed by thermal conductivity, convection and thermal radiation. Depending on the furnace design, one or another heat transfer mode may be dominant. For example, a hot plate mainly heats a sample by thermal conductivity, a diffusion furnace by thermal radiation and convection, an IR oven - by thermal radiation. In all furnaces heat is not only generated, but it is also dissipated. As a result, the sample temperature is controlled by thermal balance between the heating and cooling processes.

Additionally, the sample thermal parameters (emissivity, thermal conductivity and heat capacitance) and sample arrangement in a furnace (position, holder design and shields) affect the heating process dynamics and the sample temperature. The most complicate situation happens in the instance of phase transition of the heated thin film, e.g., melting or recrystallization. As a consequence, the sample emissivity is changed and the new thermal balance is installed.

In this paper, we demonstrate that identical heating ramp, temperature and time of the annealing are not sufficient

conditions for reproducibility of nanostructures fabricated by the annealing of thin silver films. We compare the designs of three annealing tools and analyze the relative strength of different heating modes in all tools. On the basis of optical properties and crystalline structure of the annealed and as-deposited samples we draw conclusions about melting and crystallization of silver nanostructures. To find the temperature field of the furnace and to estimate the real sample temperature we simulate the heating process in the diffusion furnace for different gas flows and sample emissivities. The obtained results are used to find correlation between annealing conditions and properties of silver nanostructures.

III. EXPERIMENTS

Four identical samples were prepared to compare annealing in different furnaces. For this purpose, a 12 nm thick silver film was deposited by electron beam evaporation at a rate 0.2 nm/s. As a substrate was used a 4" silicon wafer with 21 nm layer of thermal oxide. After the deposition the whole wafer was cut in four quotas, which were further processed separately. Annealing was done at 400 ºC during 5 minutes with a heating ramp of 21 ºC/min, and a cooling ramp of 3.6 ºC/min. However, all samples were processed in various furnaces (Fig. 1).

The sample #1 was annealed in the diffusion furnace (Fig. 1a). A 4" silicon wafer on a quartz boat was used as a sample holder, which was located in the centre of the furnace during the experiment. It was assumed that heat exchange through the quartz boat was negligible. The quartz furnace tube had a 4½ inch diameter, was 96 cm in length and with 3 mm thick walls. The resistive heater (orange strips in Fig. 1a) was situated around the tube with a gap of 1 cm. The furnace temperature was controlled according to thermocouple measurements on the tube surface. Room temperature nitrogen with a flow of 8.3×10^{-5} standard m^3/s was introduced in the furnace along its axis.

The sample #2 was annealed in a fast ramping furnace (Fig. 1b). The temperature, gas flow and process duration were the same as in the diffusion furnace (Fig. 1a). However, in the fast ramping furnace the quartz tube length was 35 cm and the sample position was close to the exhaust of the furnace. Tungsten lamps were used as heaters. The quartz tube was covered by a heat absorbing shield (black lines in Fig. 1b). The gas temperature in the tube was measured by thermocouple and was used for process control. Nitrogen was introduced through an array of holes in the right part of the furnace.

The sample #3 was annealed between two hot plates in vacuum (Fig. 1c). The diameter of both hot plates was 10 cm and they were separated by a 2.5 mm gap. The chamber wall temperature was close to room temperature.

The sample #4 is deposited silver film. The silver films were deposited in the e-beam evaporation system IM-9912 (Instrumentti Mattila Oy) at a base pressure of 2.7×10^{-5} Pa and at room temperature of the substrate. Annealing of the sample #1 was done in the diffusion furnace THERMCO Mini Brute MB-71. Annealing of the sample #2 was done in the fast ramping furnace PEO-601 from ATV Technology GmBH. Annealing of the sample #3 was done in the wafer bonder AML AWB-04 from Microengineering Ltd.

For selective etching of the samples were used diluted nitric acid (HNO_3 min. 69% from Honeywell) HNO_3:H_2O = 1:1 and diluted buffered hydrofluoric acid (BHF) BHF:H_2O = 1:3. As BHF was used standard ammonium fluoride etching mixture AF 90-10 LST from Honeywell. Two small

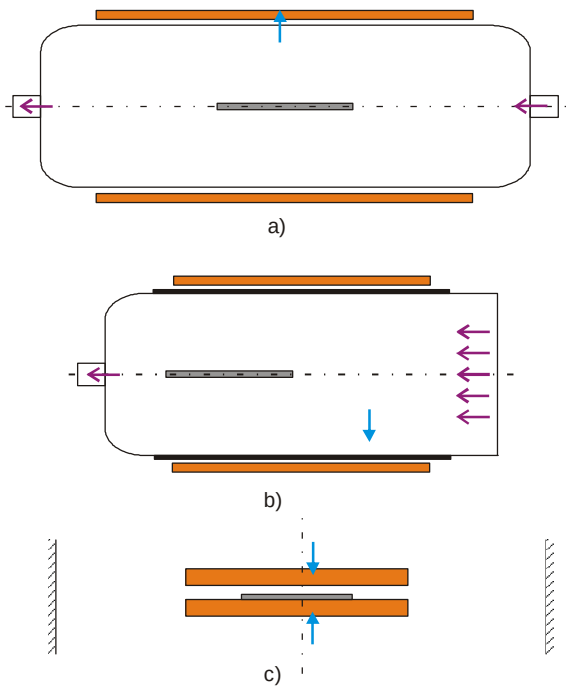

Figure 1. Design of the diffusion furnace (a), the fast ramping furnace (b) and the hot plate (c). Thermocouple positions and gas flows are denoted by blue and vilolet arrows, respectively. Heating surfaces are orange.

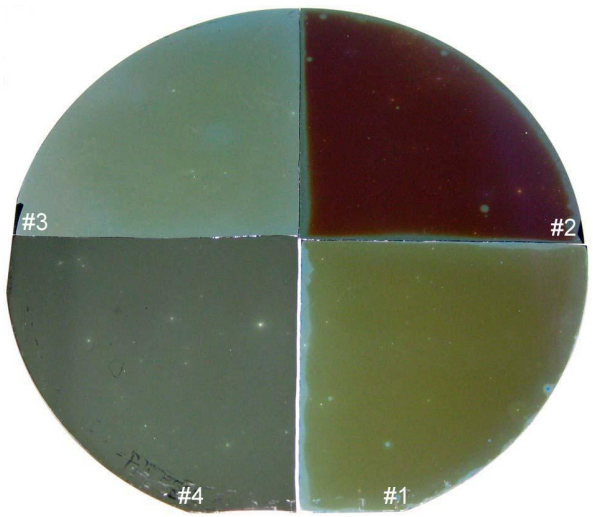

Figure 2. Optical images of the annealed (#1 - #3) and as-deposited (#4) samples.

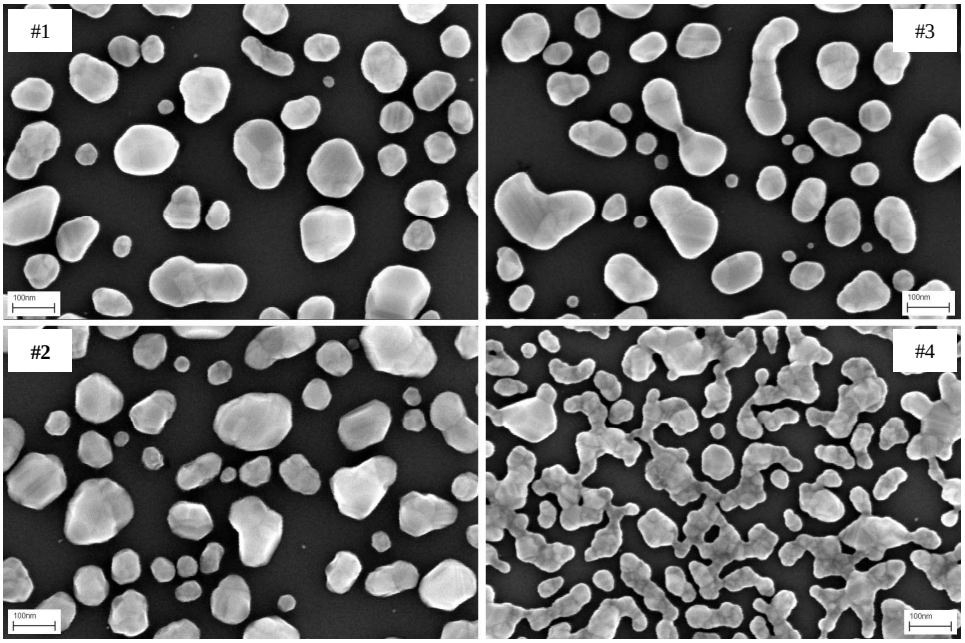

Figure 3. Plan view SEM images of the annealed (#1 - #3) and as-deposited (#4) samples.

chips (1×1 cm^2) were prepared from every annealed sample. The first chip was etched by diluted HNO_3 during 50 seconds without preliminary treatment (HNO_3 processing), the second one was dipped in diluted BHF for 10 seconds, rinsed in deionized water, dried by nitrogen and etched by diluted HNO_3 during 50 seconds (BHF/HNO_3 processing).

Plan view and tilted SEM images of the samples were observed with the Zeiss Supra 40 field emission scanning electron microscope. Reflectance measurements were carried out using the FilmTek 4000 reflectometer in the spectral range of 400–1700 nm or the spectrometer Axiospeed FT (Opton Feintechnik GmbH) in the range of 400–750 nm. Spectroscopic ellipsometry and reflectance measurements in the range of 650–1700 nm were done by spectroscopic ellipsometer SE 805 (SENTECH Instruments GmbH). The crystalline structure of the silver films was estimated by RHEED (reflection high-energy electron diffraction) observations with the help of the diffractometer embedded in a molecular beam epitaxy tool. EDS (Energy-Dispersive X-ray Spectroscopy) analyses were done with the help of a Genesis Apex 4i EDS system.

IV. RESULTS

Fig. 2 shows the optical image of three annealed samples (#1–#3) and deposited silver film (#4). The picture was taken with a digital camera with a flash. Despite identical temperature and time of annealing all samples have different colored surfaces. The sample #1 is yellow-green, the sample #2 is brown-red, the sample #3 is yellow-blue and the as-deposited sample is grey. Bulk silver is a perfect reflector, however, nanostructured silver possesses plasmon resonances, which modify reflection spectra of the samples [7, 9, 10]. Therefore, the obtained colour variation could be explained by silver nanostructures formed on the sample surface instead of the continuous film. For a detailed understanding of the effect of annealing conditions on film transformation, the structure and optical properties of the prepared samples were studied by SEM, spectroscopic ellipsometry and reflectometry.

A. Morphology of silver nanostructures

To justify the formation of silver nanostructures all samples were observed in SEM (Fig. 3). The as-deposited silver film (sample #4) is already discontinuous and has lace like structure. Silver covers a relatively large part of the sample surface in comparison with annealed films. The annealed samples have close values of silver areal density and nanostructure sizes, but the shape of the nanoislands depends on annealing conditions. The sample #2

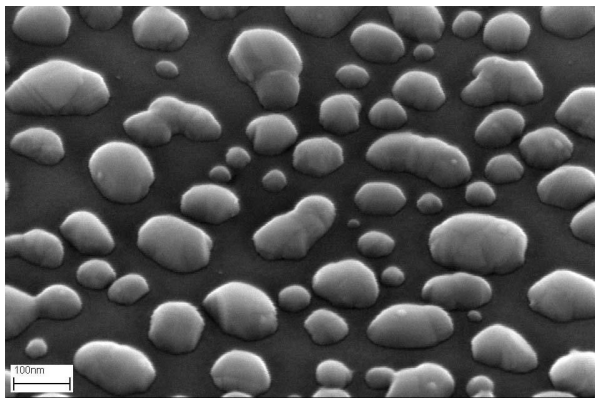

Figure 4. Tilted SEM image of the sample #2.

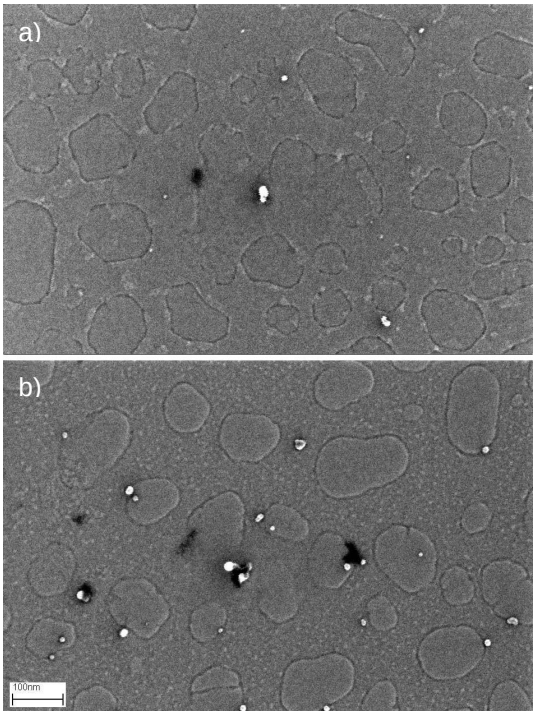

Figure 5. Plan SEM images of the sample #2 after HNO_3 (a) and BHF/HNO_3 (b) treatments, respectively.

demonstrates the most irregular islands with straight flats on some of them. The sample #3 has roundish nanostructures with large shape deviation and the sample #1 shows an intermediate picture between the previous cases. The tilted SEM image of the sample #2 is shown in Fig. 4. The silver islands have the shape of a distorted and bended ellipsoid with a flat bottom. The height of all annealed nanostructures is around 30 nm.

To investigate the modification of the SiO_2 layer below the silver nanostructures after annealing we selectively removed Ag by diluted nitric acid. The acid does not react with Si and stoichiometric SiO_2. The etched samples were studied by SEM and spectroscopic ellepsometry. SEM investigation of samples #1, #3 and #4 did not reveal anything on the sample surfaces. However, SEM images of HNO_3 and BHF/HNO_3 processed chips from the sample #2 demonstrate surface modification (Fig. 5a and Fig. 5b). The SEM plan view taken in the “in lens” mode shows dark contours of nanostructures on the lighter background. In the “in lens” tilted image and plan view taken in the “secondary electrons” mode, the mentioned contours were not observed. The surface of the sample #2 was also scanned by an atomic force microscope and contours were not found. “In lens” mode provides better resolution, but it is more sensitive to electrical charge on the sample surface than “secondary electrons” mode. Therefore, we can conclude that the black contours in Fig. 5 coincide with electrical charge variation, which in turn appears due to changing of local chemical

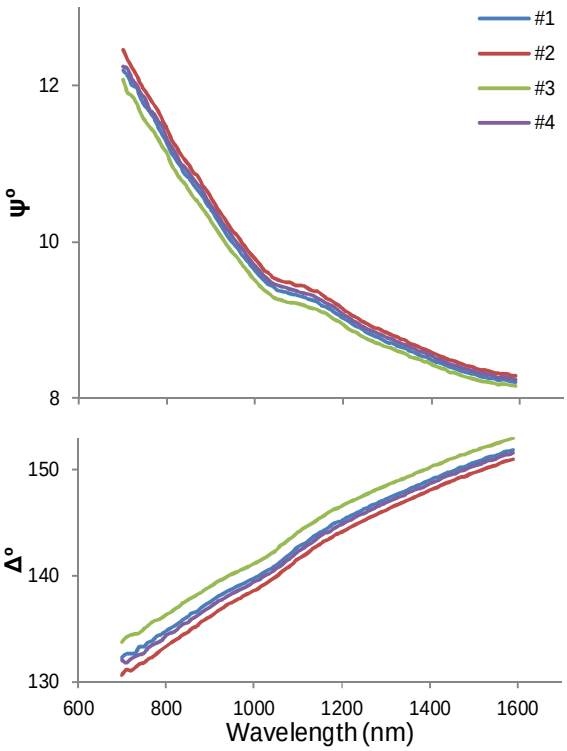

Figure 6. ψ, Δ spectra at 70° after HNO_3 treatment.

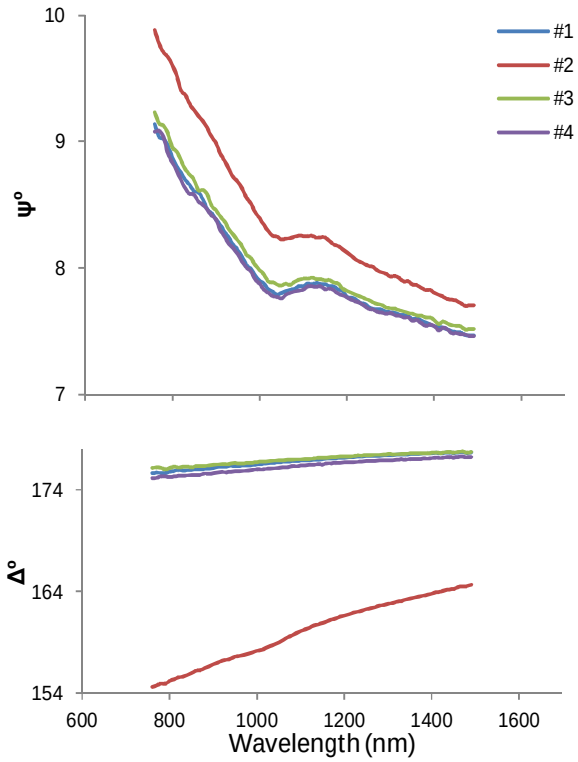

Figure 7. ψ, Δ spectra at 70° after BHF/HNO3 treatment.

TABLE I. SAMPLE DETAILS

Sample	SiO2 sublayer details after HNO3 processing					Original peak, nm	BHF peak, nm	Blueshift, nm
	Thickness, nm	*h1, nm*	*h1 composition*	*h2, nm*	*Thickness loss, nm*			
#1	18.8	12.2	SiO_2	6.6	2.2	439	425	14
#2	19.1	12.6	2% of Si in SiO_2	6.5	1.9	494	443	51
#3	17.6	10.5	SiO_2	7.1	3.4	430	411	19
#4	18.6	11.4	SiO_2	7.2	2.4	-	-	-

composition. Contours in Fig. 5b are more contrast and smoother than in Fig. 5a. Furthermore, there are bright spots in the field of Fig. 5b, which can correspond to the pinholes in the silicon oxide layer.

The RHEED showed relatively sharp, continuous Laue circles in addition to amorphous background patterns for the sample #3. Therefore, this sample contains separate crystalline particles, but their orientation varies from island to island [11]. For other samples, the intensity and sharpness of the diffraction patterns were weaker and decreased in the following order: sample #1, as-deposited sample, sample #2. In other words, the sample #2 contains nanoislands with the most disordered crystalline structure.

B. Properties of oxide sublayer

Spectroscopic ellipsometry is based on measurement of ellipsometric angles ψ, Δ for different wavelengths. The sample is described by a simplified model from several optical layers and ψ, Δ are calculated for the model. After that the matching between measured and calculated ψ, Δ is done for different parameters of the optical layers. Unfortunately, this approach is valid only for systems described by Fresnel equations. Silver nanostructures cause light scattering requiring application of Mie theory [12] and cannot be simulated by Fresnel equations. However, samples with removed silver, i.e., a Si substrate with residual SiO_2 layer can be analyzed by spectroscopic ellipsometry.

The obtained spectra of ψ, Δ after HNO_3 and BHF/HNO_3 treatments are given in Fig. 6 and Fig. 7, respectively. The samples after HNO_3 processing demonstrate small difference in ψ, Δ spectra (Fig. 6). However, BHF/HNO_3 processing results in a big difference between spectrum of the sample #2 and other spectra (Fig. 7). The reconstruction of the sample layers after HNO_3 and BHF/HNO_3 treatments was done using the optical models shown in Fig. 8a and Fig. 8b, respectively. Before this, EDS analyses were performed to ascertain the presence of silver in the etched samples. Traces of Ag were found both after HNO_3, and after BHF/HNO_3 processing. Therefore, the former SiO_2 layer is enriched by

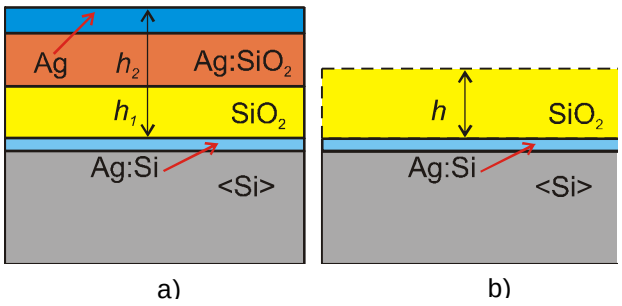

Figure 8. Optical models of oxide sublayer after HNO_3 (a) and BHF/HNO_3 (b) treatments, respectively.

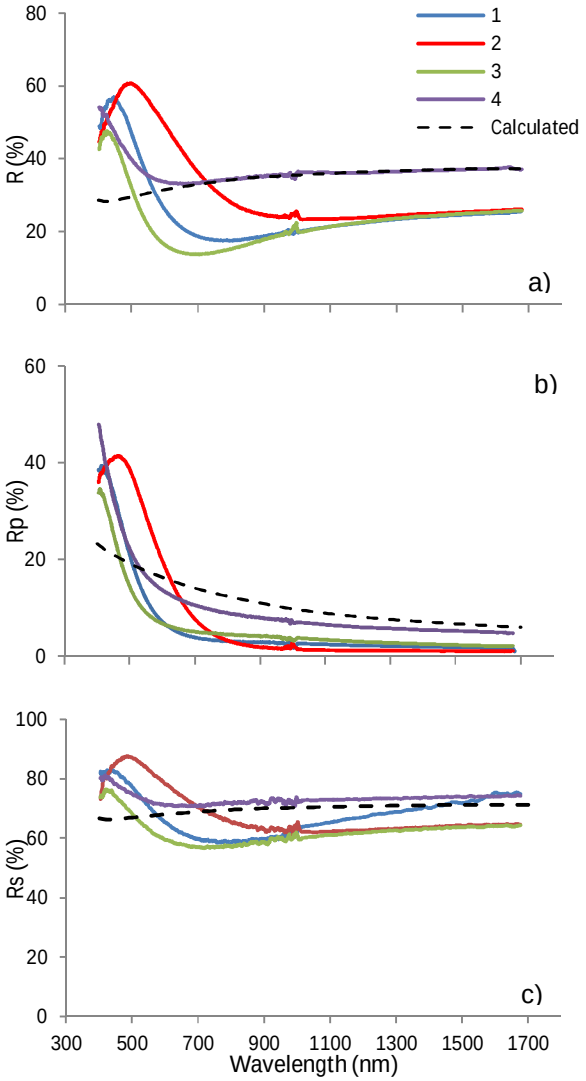

Figure 9. Reflection spectra at normal (a) and inclined (70°) light incidence for *p*-(b) and *s*- polarization (c). Dashed lines show calculated spectra.

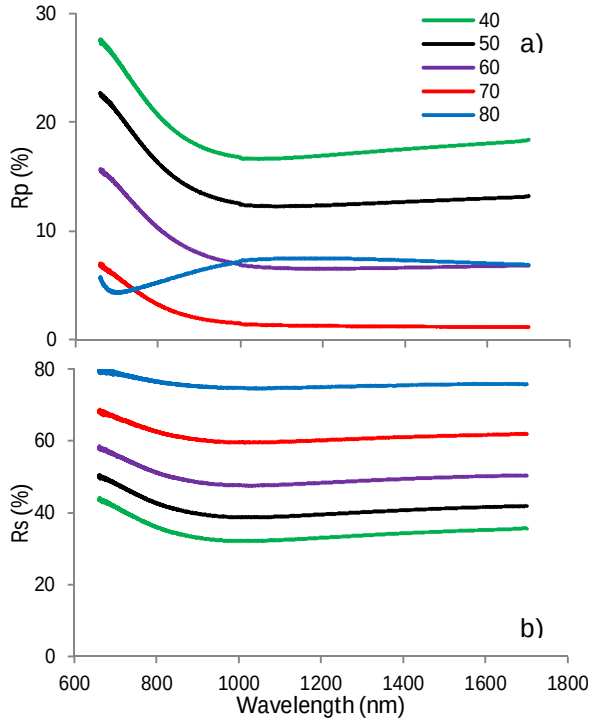

Figure 10. Reflection spectra at different angles of incidence for *p*-(a) and *s*- polarization (b).

Ag and consists of pure SiO_2 (thickness h_1) and composite Ag-SiO_2 (thickness h_2) sublayers. Additionally, a composite layer (35% of Ag in Si) with a thickness of 0.35 nm is required between the substrate and SiO_2 layer to provide the best matching (Fig. 8). The Si and SiO_2 layers with silver inclusions (Ag-Si and Ag-SiO_2) were described with the help of effective medium approximation (Bruggeman model).

The results obtained after HNO_3 processing are given in Table I. For all samples the Ag-rich layer has the same composition (11% of Ag in SiO_2). Thicknesses of the pure SiO_2 layer h_1 and Ag-SiO_2 layer h_2 are changed from sample to sample. Due to this the total thickness of oxide sublayer after HNO_3 processing is varied, but it is always less than SiO_2 thickness (21nm) before Ag deposition. The highest thickness loss was observed in the sample #3 (Table I). The sample #2 differs from others by the presence of Si-rich oxide (2% of Si in SiO_2) instead of stoichiometric SiO_2.

After BHF/HNO_3 processing the SiO_2 layer in the samples #1, #3, #4 was removed and the samples turned into bare Si substrates with thin surface layers. The composition of these layers cannot be found by means of ellipsometry [13]. The sample #2 has a residual SiO_2 layer with a thickness of 10.0 nm and an Ag-Si layer (19% of Ag in Si) at the interface with a thickness of 0.15 nm.

C. Optical properties

It has been already mentioned that colour variation of the samples could be explained by their reflection spectra, which are connected with plasmonic properties of the nanostructures. Fig. 9a demonstrates reflection spectra of the annealed and as-deposited samples at normal light incidence. In Fig. 9b and Fig. 9c, the same spectra are given at inclined light incidence (70°) and for *p*- and *s*- polarization, respectively. According to surface colour, the sample #2 has the main peak at the longest wavelength of 497 nm, the sample #3 at the shortest wavelength of 425 nm and the sample #1 at the intermediate wavelength of 448 nm for normal light incident (Fig. 9a). The as-deposited sample #4 has no reflection peaks in the range of the measurements, but it has trough at the wavelength of 654 nm. On the other hand, the sample #2 has no troughs at all and the samples #3 and #1 have troughs at 694 nm and 767 nm, respectively.

For *p*-polarized light strong reflection is observed only in the visible range (below 800 nm). IR reflectance falls down to 2% for all annealed samples and to 5% for the as-deposited sample. Peaks of reflection for *p*-polarization shift to shorter wavelength and for the sample #2 the peak is observed at 470 nm. For *s*-polarized light spectra of the annealed samples coincide with each other in the IR range (above 1200 nm), which justifies the suggestion concerning identical silver areal density. Blueshift of the peak positions between Fig. 9a and Fig. 9c is equal 12 nm for samples #2,#3 and 4 nm for the sample #1, respectively.

Angle dependence of reflection was studied in near IR range. Fig. 10 demonstrates the reflectance of the sample #2 (the behavior of other samples is similar) for both polarizations in the range of 650–1700 nm. Reflectance of *p*-polarized light falls down with increasing the incident angle

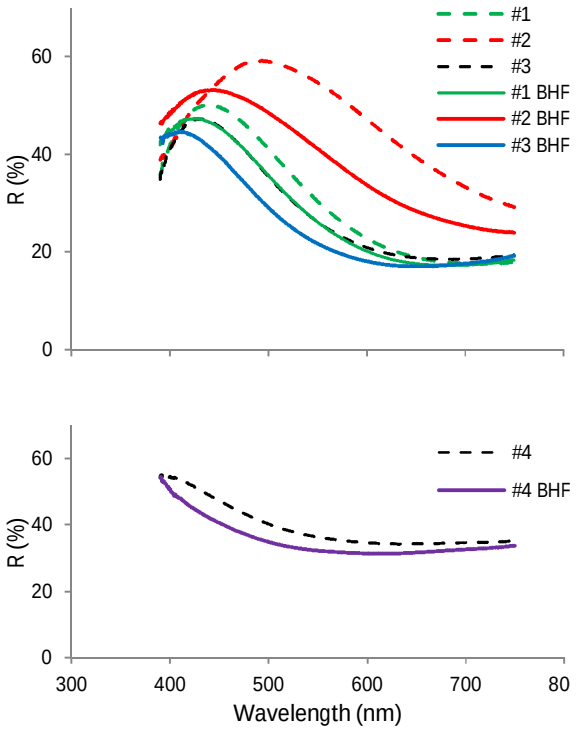

Figure 11. Reflection spectra at normal light incidence before and after BHF treatment.

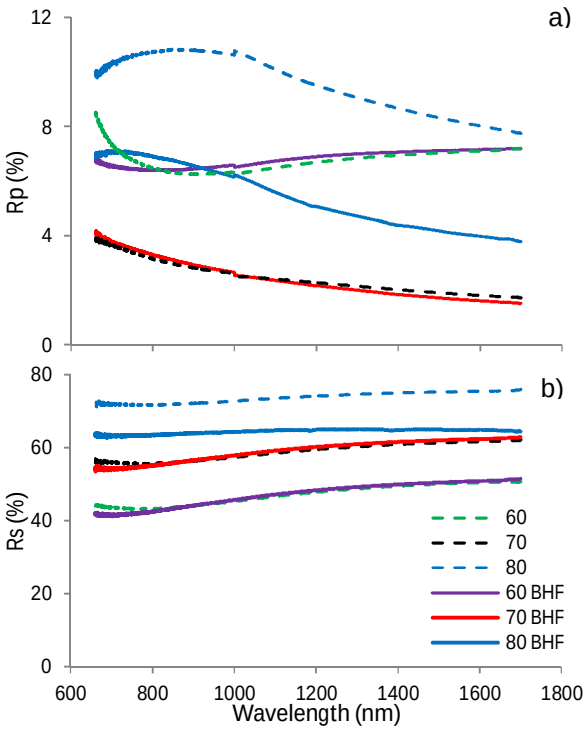

Figure 12. Reflection spectra at different angles of incidence before and after BHF treatment for *p*-polarisaion (a) and *s*-polarization (b).

and reaches its minimum at 70º. After that the wavelength behavior of reflection is changed and the spectrum at 80º looks like a mirror reflection of the 60º spectrum. At the same time, trough positions are redshifted with increasing incident angle. For *s*-polarization the spectrum shape and trough position (1050 nm) are independent from the angle of incidence and reflectance intensity growths with increasing the incident angle.

In IR range scattering is negligible and sample reflection can be described by Fresnel equations. The proposed model consists of a 21 nm thick oxide layer and a Bruggeman Ag-air layer. Reflectance spectra of the sample #4 were used for matching with the optical model, because its silver layer is closest to a continuous film. It was found that the sample #4 can be approximated by a 37 nm thick Ag-air layer (31.5% of Ag). Dashed lines in Fig. 9 show spectra calculated with the help of the obtained model.

For one set of samples (#1–#4) BHF/HNO_3 processing was stopped after BHF etching. After that the SEM investigation did not show any difference between BHF processed and just annealed samples. However, reflectance spectra of all samples were modified in a similar way (Fig.11). After BHF processing the spectrum peaks were shifted to shorter wavelengths and their intensity decreased (Table I).

Reflectance in IR range is not sensitive to BHF processing, excluding the angle of incidence 80º and *p*-polarization (Fig. 12). The spectrum for this angle is shifted down (reflectance decreased) and preserves invariable shape.

D. Simulations

The purpose of simulations in this work is to find out the effect of different heat transfer modes on sample heating in the diffusion furnace (Fig. 1a). 3D simulations of the annealing process were done with the help of software COMSOL Multiphysics 3.5a. Gas flow in the furnace is non-isothermal, which assumes the coupling of fluid dynamics and heat transfer equations in the whole volume of the 96 cm long furnace. Preliminary simulations demonstrate that a converging solution can be obtained for mesh element size less than 5 mm near the surface of the heated wafer (it is the most problematic place for modeling). In this case, the required numbers of mesh elements and degrees of freedom are 70000 and 455000, respectively. The corresponding solution time and memory use for this model are tens of hours and 15 Gb, respectively. However, finding suitable mesh parameters and proper stabilization techniques requires multiple attempts, which leads to high computational load and makes this approach unpractical.

Taking the above mentioned into consideration, the simulations were done in two phases. Firstly, the temperature and velocity fields inside the empty furnace were found. For this purpose two transient models were used in coupled mode: a general heat transfer model and a weakly compressible Navier–Stokes model for non-isothermal flow. The first one calculates gas temperature distribution in the furnace volume due to thermal conduction and convection. Boundary conditions are a fixed temperature of 400 ºC for quartz tube walls and room temperature for input gas. At the gas outlet from the furnace heat exchange was provided by

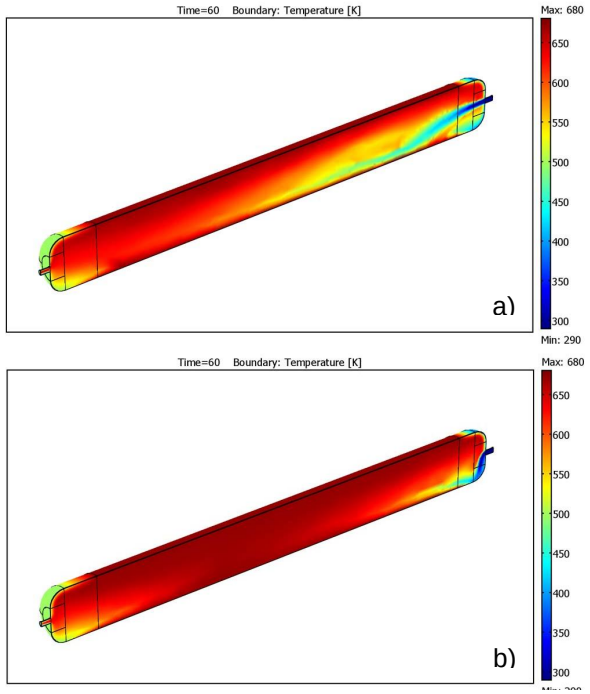

Figure 13. Temperature fields of the diffusion furnace for high (a) and low (b) nitrogen flows. The gas inlet is on the right.

convective flux. The second model calculates gas velocity distribution in the furnace volume caused by inlet pressure and non-uniform temperature. Boundary conditions are laminar inlet flow and atmospheric pressure without viscous stress at the outlet. Appeared gravitational force due to gas density variation was taken into account as the vertical volume force.

At the second phase, the obtained temperature and velocity of gas were used as inlet boundary conditions for the simulation of silicon wafer heating in the hot cylindrical tube. The rest of the boundary conditions were the same as at the first phase. All heat transfer modes, including sample, tube and gas thermal conduction, convection in nitrogen and surface-to-surface radiation were taken into account.

Fig. 13 demonstrates the simulation results obtained at the first phase. Temperature distributions in the diffusion furnace were calculated for the quartz tube with a temperature of 400 ºC and for gas flows 8.3×10^{-5} standard m^3/s (Fig. 13a) and 1.0×10^{-5} standard m^3/s (Fig. 13b), respectively. The large flow of cold gas creates non-uniform temperature distribution inside the tube and gas temperature in the middle of the furnace (below the sample holder) can be 150 ºC lower than the tube temperature (Fig. 13a). At the same place gas velocity reaches a maximum value of 0.18 m/s. At the small flow of nitrogen (Fig. 13b), temperature variation and gas velocity in the centre of the furnace do not exceed 15 ºC and 0.03 m/s, respectively.

Temperature and velocity fields near the wafer are illustrated in Fig. 14a and Fig. 14b, respectively. They are obtained at the second phase of simulations (temperature and

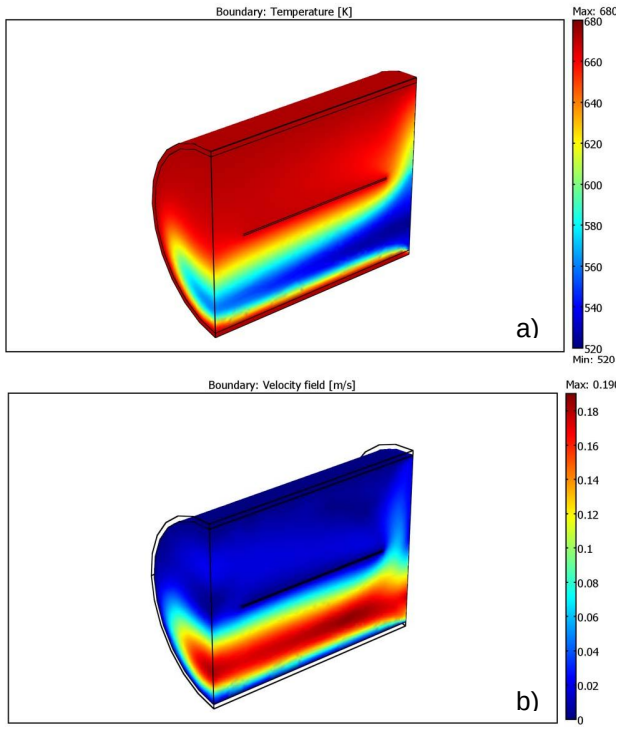

Figure 14. Temperature (a) and velocity (b) fields near the wafer for high nitrogen flow and ε=1. Gas moves from right to left.

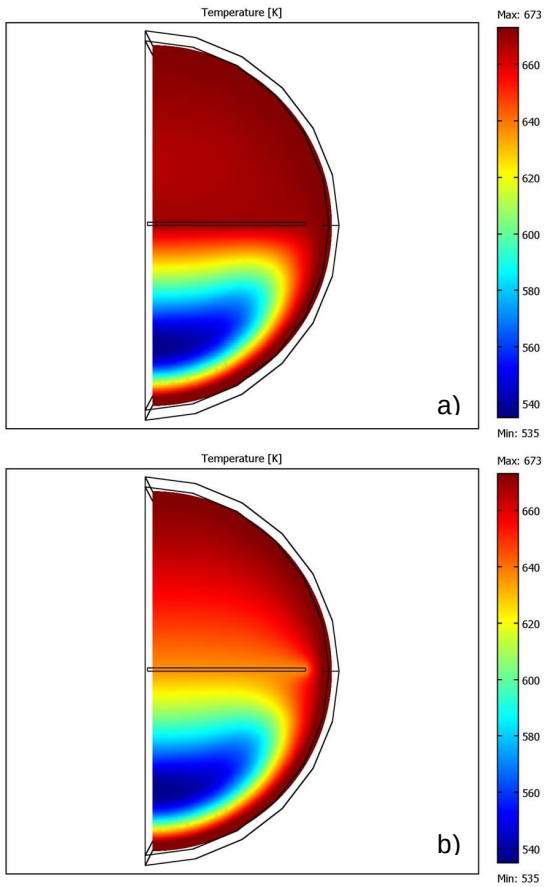

Figure 15. Vertical cross sections of the temperature field at high nitroghen flow in the centre of the furnace for ε=1 (a)and ε=0 (b).

velocity of the gas at the entrance are taken from Fig. 13a) for nitrogen flow 8.3×10^{-5} standard m^3/s and sample emissivity ε=1. The internal furnace volume is divided by the wafer holder in two parts – the upper one with high temperature and low velocity and the lower one with low temperature and high velocity. In the upper volume gas has a temperature of 398 ºC and slowly moves with a velocity of 0.02 m/s. In the lower volume high temperature and velocity gradient exist. However, the wafer temperature variation does not exceed 1ºC due to high thermal conductivity of silicon. In the present experiment, the wafer temperature depends on tube temperature, nitrogen flow and wafer emissivity ε. Cross sections of the temperature fields in the centre of the furnace for ε=1 and ε=0 are given in Fig. 15a and Fig. 15b, respectively. The temperature of the heat absorbing sample (ε=1) is 35 ºC higher than the temperature of the reflective sample (ε=0). As a consequence, the temperature distribution in the upper volume is more uniform for ε=1.

V. DISCUSSION

Annealing of thin silver films is complicated due to three circumstances. Firstly, silver films and nanostructures are melted at low temperatures [5, 14, 15]. In our previous study

[7], it was shown that this melting point is close to 250 ºC. However, this transformation happens only once and the second heating of the sample does not change morphology of the silver nanostructures. Secondly, liquid silver has a tendency to form spherical shapes of nanoislands due to low cohesive forces to SiO_2 surface. Thirdly, silver is the best plasmonic material [9] and the silver nanostructures appeared after breaking apart the continuous film, modify optical properties of the sample surface [10].

The first sign of not identical annealing conditions in the studied furnaces is different sample colours (Fig. 2) and the corresponding changing of reflection spectra after annealing (Fig. 9). The reflection spectra demonstrate strong plasmon properties of the silver nanostructures formed after silver film annealing. The troughs in the range 690–1050 nm correspond to dipole plasmon resonance and peaks at 410–500 nm correspond to quadrupole resonance [10]. The non-annealed sample #4 possesses only very weak dipolar plasmon resonance (see spectrum of as-deposited sample).

The second consequence of not identical annealing is variation in chemical composition and thickness of the oxide sublayer below the silver nanostructures from sample to sample. The resulting thicknesses of the SiO_2 and Ag-SiO_2 layers (Table I) obtained after HNO_3 processing are defined by concentration and distribution of silver in the oxide matrix (Fig. 8). Nitric acid cannot remove silver from SiO_2, if silver concentration is below the corresponding threshold (11% in our samples). Due to this, the Ag-SiO_2 layer left after etching has a silver concentration below 11% (Fig. 8). Therefore, the uppermost Ag-rich SiO_2 (more than 11% of Ag) is removed and thickness loss is higher for samples with higher Ag concentration. The sample #3 has maximal thickness loss and contains maximum amount of silver in oxide.

The sample #2 has minimal thickness loss and contains 2% of excess Si in the lower part of the oxide sublayer (Table I). On the other hand, the sample #2 demonstrates black contours after HNO_3 processing (Fig. 5). One might suppose that excess silicon may be concentrated in these contours, corresponding to removed Ag islands. Electrical field of plasmon oscillations is strongest along the contact line between silver and oxide. Therefore, Si enrichment may be connected with light stimulated diffusion around contact line. Furthermore, silicon can diffuse through deposited silver and can be oxidized on top of it [16]. In our case it means that Si can diffuse through the interface Ag-Si layer (Fig. 8) and is oxidized on top of it. Both light stimulated diffusion and interface stimulated diffusion can lead to compensation of thickness loss.

Section III mentioned that *p*-polarized light is reflected in different way for small (less than 70º) and large (more than 70 º) angles of incidence. We believe that it can be related to Brewster's angle of silicon (74º at 1200 nm) and there are two reasons for this. Firstly, *p*-polarized light is not reflected, but only refracted at Brewster's angle. This was observed in our measurements at 70º (Fig. 9b). Only in this configuration the right position of quadrupole resonance can be visible, because the scattering from silver nanostructures is not disturbed by the reflection from the substrate. Secondly,

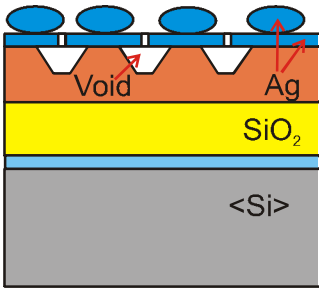

Figure 16. Void layer formation after BHF processing.

there is a jump in the reflection phase at Brewster's angle, i.e., for smaller angles of incidence original and reflected lights have a phase shift of 180º, but for larger angles the phase shift is 0º. It is illustrated by distinguished behavior of the reflection spectrum for 80º in Fig. 10a. Therefore, reflection from Si/SiO_2 interface plays a crucial role in modification of the observed spectra and redshift of troughs for *p*-polarized light with increasing of the incident angle may be explained by destructive interference (Fig. 10a).

To some extent plasmon properties can be estimated by the difference between calculated Fresnel equations and measured spectrum, i.e., the larger difference, the stronger plasmon resonance. Based on this criteria, the strongest plasmon resonances are observed in the samples #1 and #3 (Fig. 9).

In Section III, we have shown that all annealed samples have similar values of silver areal density and nanostructure sizes. Therefore, relatively large redshift of peaks and troughs in Fig. 9 cannot be only explained by the changing of island geometry. Due to the identity of the studied samples, the spectrum variations can be also connected with material modification, e.g., changing of Ag or SiO_2 dielectric functions. Spectral peak and trough broadening (sample #2 has the broadest peak) tells about an increase of the imaginary part of Ag dielectric function. Peak shift is connected with changing of a real part of the dielectric function, i.e., refractive index [9, 12]. It is clearly demonstrated by blueshift of plasmon resonances in the experiment with BHF etching (Fig. 11 and Table I). Due to pinholes in silver residues between the nanostructures (Fig. 16), SiO_2 is partially etched and voids are formed below the Ag nanostructures. It results in decrease of the effective refractive index n of the substrate (n_{air}=1, n_{SiO2}=1.45) and a corresponding shift of the plasmon resonance. Additionally, the same voids can increase scattering of the light travelling in the SiO_2 layer, which leads to uniform decrease in intensity of the light reflected at 80º (Fig. 12).

Typically, annealing is used to improve and restore crystalline structure. However, there are reports about increased defect concentration in melted silver samples [17]. Our RHEED observations also showed that the crystalline structure of the annealed sample #2 is worse than the structure of the as-deposited one. Taking into account the broadest reflection peak and the absence of a dipolar trough in the sample #2, we can conclude that this sample has the

highest disorder of crystalline structure among the studied samples.

In the diffusion furnace (Fig. 1a) the target temperature 400 ºC was supported on the external side of the quartz tube. In the fast ramping furnace (Fig. 1b) the target temperature 400 ºC was supported inside the furnace, at 1cm above the bottom of the quartz tube. According to Fig. 14a, the measured temperature in this point can be 150 ºC lower than the tube temperature, i.e., in our experiment the tube temperature of the fast ramping furnace could be close to 550 ºC. Nitrogen flow 8.3×10^{-5} standard m^3/s is very low for the fast ramping furnace (Fig. 1b) and provides laminar gas flow inside the tube. In the case of the diffusion furnace (Fig. 1a), the same nitrogen flow is too high and provides turbulent gas flow in the lower part of the tube (Fig. 13a). Higher temperature of the absorber shield (ε~1) around the quartz tube makes thermal radiation in the fast ramping furnace much higher than in the diffusion one.

In the case of a thin silver layer on silicon, most of radiation energy is absorbed in the silver and during heating up in the laminar gas flow (the fast ramping furnace) the silver temperature is higher than the temperature of the substrate. In turbulent gas flow (the diffusion furnace), intensive heat exchange between the silver and nitrogen prevents overheating of the silver nanostructures.

After melting silver starts to form droplets due to surface tension forces and decreases silver areal density. However, absorbed thermal radiation is proportional to silver areal density or absorbing cross-section. Thus, geometry change decreases radiative heat transfer to the silver. The cold substrate cools down silver nanostructures and causes their rapid solidification. The quenching happens without proper crystallization and silver solidifies in amorphous phase (sample #2).

In the case of low radiative heat transfer (samples #1, #3), melting happens at higher substrate temperature and without silver overheating. Depending on conductive and radiative heat fluxes the melted silver is cooled with a much lower rate and solidifies in polycrystalline phase. In our study, the sample #3 has the best crystalline structure due to lower cooling rate between two hot plates in vacuum. One of the reasons for quenching in this case is the reduction of the surface energy [18]. Another reason is the heating of silver nanostructures by conductive flux through thermal contact with substrate. Silver melting acquires additional heat flux from the substrate to the nanostructure. This heat flux increases the temperature drop on the interface between the substrate and the silver droplet, which in turn leads to decreasing of the silver temperature and quenching.

VI. Conclusion and Future Work

Annealing of identical samples at identical times and temperatures, but in different furnaces leads to different results. We have demonstrated that optical properties and morphology of silver nanostructures produced by annealing of thin film are very sensitive to the heat delivering method. Relative strength of the heat transfer modes affects the wavelength of plasmon resonance, nanostructure geometry and chemical composition of the oxide sublayer. The effect of furnace operational parameters (gas flow, sample and thermocouple position, sample and environment emissivity) on annealing results has been confirmed. Radiation heating of silver can be very strong and provides overheating of film with regards to the substrate. It results in silver melting and droplet formation. The appearing of nanostructures and shrinking of silver areal density lead to a decrease of radiation heating. As a result, melted structures are quenched to solid state with irregular shape and high crystalline disorder. The effect depends on the rate of solidification and explains the variation of annealing results from furnace to furnace.

The results presented here have demonstrated the significance of all furnace operational parameters and can be used for controllable heat processing of different materials. However, the work can be further developed for various furnace designs and thin film materials. Furthermore, accuracy and validity of the process simulations can be improved. Proper understanding of film transformation during annealing opens an effective way for the formation of nanostructures of different shapes, e.g., arrays of spherical nanoislands.

Acknowledgment

This research was undertaken at the Micronova Nanofabrication Centre of Aalto University.

References

[1] V. Ovchinnikov, “Analysis of Furnace Operational Parameters for Controllable Annealing of Thin Films,” Proceedings of ICQNM 2014, ThinkMind Digital Library (ISBN: 978-1-61208-380-3), pp. 32-37.

[2] Handbook of Semiconductor Manufacturing Technology, 2nd edition edited by R. Doering and Y. Nishi, CRC Press, 2007, 1720p.

[3] S. Franssila, “Introduction to Microfabrication,” 2nd edition, Wiley, 2010, 534p.

[4] V. Ovchinnikov, A. Malinin, S. Novikov, and C. Tuovinen, ”Silicon Nanopillars Formed by Reactive Ion Etching Using a Self-Organized Gold Mask,” Physica Scripta, vol.T79, 1999, pp. 263-265.

[5] S. R. Bhattacharyya et al., “Growth and Melting of Silicon Supported Silver Nanocluster Films,” J. Phys. D: Appl. Phys., vol. 42, 2009, pp. 035306-1 - 035306-9.

[6] D. Adams, T. L. Alford, and J. W. Mayer, “Silver Metallization: Stability and Reliability,” Springer, 2008, 123p.

[7] V. Ovchinnikov, “Effect of Thermal Radiation during Annealing on Self-organization of Thin Silver Films,” Proceedings of ICQNM 2013, ThinkMind Digital Library (ISBN: 978-1-61208-303-2), pp. 1-6.

[8] D. Guo, S. Ikeda, K. Saiki, H. Miyazoe, and K. Terashima, “Effect of annealing on the mobility and morphology of thermally activated pentacene thin film transistors,” J. Appl. Phys., vol. 99, 2006, pp. 094502-1 – 094502-7.

[9] M. A. Garcia, “Surface Plasmons in Metallic Nanoparticles: Fundamentals and Applications,” J. Phys. D: Appl. Phys., vol. 44, 2011, pp. 283001-1 - 283001-20.

[10] V. Ovchinnikov and A. Shevchenko, “Self-Organization-Based Fabrication of Stable Noble-Metal Nanostructures on Large-Area Dielectric Substrates,” Journal of Chemistry, vol. 2013, 2013, Article ID 158431, pp. 1 - 10., http://dx.doi.org/10.1155/2013/158431.

[11] A. Ichimiya and P. I. Cohen, “Reflection High-Energy Electron Diffraction,” Cambridge University Press, 2004, 353p.

[12] E. C. Le Ru and P. G. Etchegoin, “Principles of Surface-Enhanced Raman Spectroscopy and Related Plasmonic Effects,” Elsevier, 2008, 688 p.

[13] H. G. Tompkins, “A User's Guide to Ellipsometry,” Academic Press, 1993, 260p.

[14] O. A. Yeshchenko, I. M. Dmitruk, A. A. Alexeenko, and A. V. Kotko, “Surface Plasmon as a Probe for Melting of Silver Nanoparticles,” Nanotechnology, vol. 21, 2010, pp. 045203-1 - 045203-6.

[15] M. Khan, S. Kumar, M. Ahamed, S. Alrokayan, and M. Salhi, “Structural and Thermal Studies of Silver Nanoparticles and Electrical Transport Study of Their Thin Films,” Nanoscale Research Letters, vol. 6, 2011, pp. 434-1 - 434-8.

[16] A. Hiraki and E. Lugujjo, “Low-Temperature Migration of Silicon in Metal Films on Silicon Substrates Studied by Backscattering Techniques,” J. Vac.Sci.Technol., vol. 9, 1972, pp.155-158.

[17] S. A. Little, T. Begou, R. E. Collins, and S. Marsillac, “Optical Detection of Melting Point Depression for Silver Nanoparticles via in situ Real Time Spectroscopic Ellipsometry,” Appl. Phys. Lett., vol. 100, 2012, pp. 051107-1 -1 051107-4.

[18] E. P. Kitsyuk, D. G. Gromov, E. N. Redichev, and I. V. Sagunova, “Specifics of LowTemperature Melting and Disintegration into Drops of Silver Thin Films,” Protection of Metals and Physical Chemistry of Surfaces, vol. 48, 2012, pp. 304–309.